

Estimation of the optimal parameters for K-edge subtraction imaging with PixiRad-2/PixieIII photon counting detector on a conventional laboratory X-ray micro-tomograph.

R. Granger^{a,b} L. Salvo^b S. Rolland Du Roscoat^a P. Lhuissier^b

^aUniv. Grenoble Alpes, CNRS, Grenoble INP¹, 3SR, UMR 5521, F-38000 Grenoble, France

^bUniv. Grenoble Alpes, CNRS, Grenoble INP¹, SIMAP, F-38000 Grenoble, France

E-mail: remi.granger@univ-grenoble-alpes.fr,
pierre.lhuissier@simap.grenoble-inp.fr

ABSTRACT: Photon Counting Detectors (PCDs) open new opportunities in X-ray imaging. Pixie III is a PCD using simultaneously two energy thresholds. This enables to acquire images from two distinct energy bins in a single exposure. This is particularly suited to perform K-Edge Subtraction (KES) imaging with laboratory sources. In that context, one has however to deal with an energy bin optimization: narrow energy bins leads to high KES signal, at the expense of higher noise, while wider energy bins leads to poor KES signal but better statistics. This work presents a model that aims at finding the optimal thresholds and source voltage in order to retrieve the best Contrast to Noise Ratio (CNR) for a given sample. The model also optimizes the configurations for conventional absorption modality and compares both modalities. We noticed that the input flux and the energy difference between the thresholds influence the noise on image. We included this in the model using phenomenological laws. The model is then compared to empirical optimization by experimental screening of the parameters on model materials composed of barium, iodine and water. Finally, a study of the predicted CNRs has function of the sample composition is presented as an example of usage of the model.

KEYWORDS: Photon counting detector, K-edge imaging, advanced noise model, contrast to noise ratio, X-ray imaging

¹Institute of Engineering Univ. Grenoble Alpes

Contents

1	Introduction	1
2	Materials	3
3	Model	4
3.1	Analytical expression of CNR	4
3.2	Source model	7
3.3	Absorption model	7
3.4	Noise model	8
4	Results	12
4.1	Resolution	12
4.2	Validation	12
4.3	Application example	15
5	Discussion	18
6	Conclusions and perspectives	19

1 Introduction

X-ray imaging and computed tomography (CT) are sets of characterization techniques daily used in a wide variety of fields. Material science, medical and biological science, industries are examples (see e.g. [1]). The conventional and most employed technique is based on absorption contrast, discriminating material by their difference of absorption at a given energy (monochromatic beam) or by their difference of integrated absorption over an energy range (with a polychromatic beam). However, it may happen that this contrast is not large enough to differentiate the materials, a possibility to enlarge contrast in that case is to exploit phase contrast relative techniques [2–4] however these techniques are not easy to handle on laboratory tomograph.

A variation of the absorption contrast approach is to build contrast from variation of absorption coefficient measured at two different energies (or over two distinct energy ranges). The interest of doing so, is to increase the contrast between two materials when one of them see its K-edge, that corresponds to a strong variation of absorption coefficient, lying between the two spectral measurements points. Thus, it is named K-edge Subtraction (KES) imaging [5]. The classical example of application is the use of contrast agent as iodine or barium in biological sample, in medical or biological context. Historically, the technique was developed under somehow monochromatic condition with laboratory source, using secondary source fluorescence peaks [6, 7] or additional monochromator [8]. This permits to perform measurements right before and right after the K-edge. However,

these approaches were restricted to specific chemical elements and limited to low flux. Practically, this technique was mainly used at synchrotron [9, 10] as the beam offer high monochromaticity and high flux at the expense of the accessibility of the technique. However, recent development of new technologies offers mean to overcome that limitation. Recently, a Compact Light Source has been employed to perform KES imaging for medical application[11]. While this kind of sources definitely offers promising perspectives, it is currently not widespread and correspond to scale of size and cost intermediates between laboratory sources and synchrotron, but still significantly larger than laboratory sources. Another strategy to develop KES imaging relies on the recent development of photon counting detectors, offering detectors with energy-discriminating capabilities [12]. One of them is the PixieIII photon counting detector [13] : it has the capacity to count incoming photons over two distinct energy ranges simultaneously, allowing to acquire two images in a single exposure time when illuminated with a polychromatic beam. This technology allows taking benefits of the polychromatic aspects of laboratory X-ray sources, and their associated advantages.

However, as in that case the absorption coefficient measurements correspond to mean over energy ranges, and not at specific energies, one has to deal with an optimization problem. This problem is depicted in figure 1. Consider two absorbance spectra of two distinct materials, one

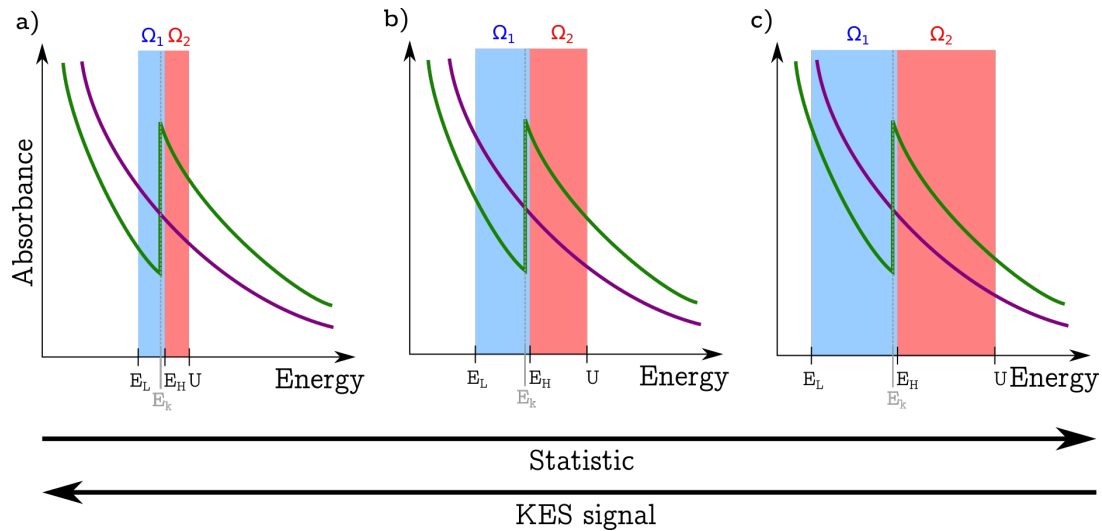


Figure 1. Scheme of the optimization problem of KES imaging with lab source. Green and purple solid curves are absorbance spectra of the two materials. a) Taking narrow energy bins: good signal, low statistic, b) large bins: good statistics, low signal, c) optimal energy bins.

with K-edge at energy E_K and another one without K-edge represented by the green and purple solid curves respectively. The detector thresholds E_L and E_H and the source voltage U defines the energy range Ω_1 and Ω_2 over which the two spectral images are formed (represented by the blue and red shaded area respectively). In order to get the strongest KES signal, one may be tempted to use narrow energy ranges on each side of the K-edge energy as sketched by figure 1.a). However, since laboratory sources offer limited photon flux, this would result in low statistic images. Inversely, in order to get lower noise, one may choose large energy bins as in figure 1.c). In this case, the KES signal is low as the averaging over large energy bin somehow smooths the K-edge. So the optimal tuning of the energy ranges over which to perform the K-Edge imaging is a trade-off between high

KES signal and good statistic in the images (fig. 1.b))

To address this problem, He et al. [14, 15] presented a theoretical approach to predict the optimal width of the energy range. Their model is based on optimization of contrast to noise ratio of the projection images, the noise being Poisson noise from the beam, and the contrast signal obtained from Beer-Lambert law through the sample. Their results assumed an equal bin width of the two energy bins. Later, Meng et al. [16] used the same approach, the optimization being based on the Contrast to Noise Ratio (CNR) of the reconstructed images, and showed that bin width are similar when optimizing CNR on projections or reconstructed images. While this approach answer to the optimization problem for the general case, detector-specific features like detector noise or spectral resolution are not taken into account. For PixieIII, Brun et al. [17] presented results of empirical optimization of one of the two thresholds on a test phantom made of iodine, water and barium. The objective of this work is to present an optimization model that includes both theoretical modelling of general behaviour of detector and empirical detector-specific characteristics (noise, spectral resolution, counter depth) in order to refine predictions when using PixieIII detector. By the way, the model aims at being as less constrained as possible, and optimizes simultaneously: source voltage and current, both energy thresholds, and predicts if it is better to use KES imaging or conventional absorption imaging for the considered sample. This paper is structured as follows. The first section presents the detector. The second section is dedicated to the model, and is divided in three sub-model : (i) a source model, (ii) a contrast model and (iii) a noise model. The third section presents results obtained with the model and compares them with experimental optimizations. Finally, the fourth section shows an application example where optimal CNRs for both absorption and KES modality are compared over a range of chemical composition of the sample.

2 Materials

PixiRad2-PixieIII is a photon counting detector with energy-discriminating capabilities. The detector is made of 2 PixieIII module tiled side-by-side and made from a 750 μm CdTe crystal bonded to a processing ASIC. This offers a grid of 1024x402 squared pixels of 62 μm . The detector offers two thresholds – that will be named low threshold, at energy E_L and high threshold at energy E_H – associated with two 15 bit counters, this enabled to acquire 2 images, on two distinct energy bins simultaneously. The so called low-energy counter counts photons with energy in range $\Omega_1 = [E_L, E_H]$ while the high energy counters count photons with energy in range $\Omega_2 = [E_H, \infty[$. The detector has the specificity to offer 3 levels of correction of charge sharing at the hardware level. Throughout this article, the detector was operated in NPISUM mode, which corresponds to the finest level of correction of charge sharing, and corrects both the number of counts, and the energy of the interaction events. ([13, 18, 19]).

For all acquisitions, we used a microfocus reflection source (HAMAMATSU L12161-07) with tungsten anode and operated with an acceleration voltage of 50 kV.

To develop the absorption model and to evaluate its performance, we used a phantom sample made with three capillary glass of 1 mm opening diameter, filled with a solution of 0.3 g/cm^3 of KI, barium sulfate a solution of 0.46 g/cm^3 of BaSO_4 and distilled water for reference (figure 2).

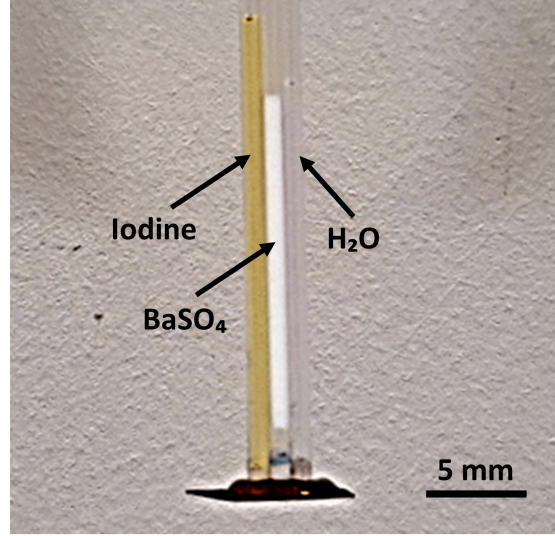


Figure 2. An example of test phantom made with three capillary glass tubes of 1 mm of inner diameter, filled with KI solution, BaSO₄ solution and water.

3 Model

The objective of the model is to help the operator to choose configuration parameters based on the sample he wants to image and the objectives of the acquisition. Given the materials A and B to be contrasted in the sample, with respective densities ρ_a and ρ_b , the model predicts the source voltage U , current i , the two detector energy thresholds (E_L and E_H) and the modality to use (absorption or KES imaging) in order to achieve the highest Contrast-to-Noise Ratio (CNR) on the obtained radiographs. Actually, current i and exposure time have equivalent influence on the variable of interest, namely it acts on the number of counted photon during exposure. Here the reasoning is done talking with current i only for simplicity, thinking exposure time as fixed. But the current variable could then be thought as the product of current times exposure time or exposure while keeping current fixed without modifying the conclusions. The objective of the model is represented by the function f in the equation 3.1.

$$(U, E_L, E_H, i, mode) = f(A, B, \rho_A, \rho_B) \quad (3.1)$$

For the context of computed Tomography, [16] showed that optimizing CNR for radiographs is close to optimizing on reconstructed images. Thus, we focused in predicting CNR on radiographs, however, as shown by relation 3.1, the objective is rather to focus on wider optimization by optimizing several parameters as the choice of these parameters are linked, and particularly, the two thresholds are optimized.

3.1 Analytical expression of CNR

The metric to evaluate CNR for a given modality MOD is defined as the difference of mean signal between material A and B divided by a standard deviation representing noise computed on the

image with that modality:

$$CNR_{MOD} = \frac{|\langle MOD_A \rangle - \langle MOD_B \rangle|}{\sigma_{MOD}} \quad (3.2)$$

Where MOD_m represent the image obtained with the modality MOD for material m, $\langle \cdot \rangle$ stand for mean of pixel values over a representative region of Interest (ROI) and σ_{MOD} is the mean of the standard deviations measured for material A and B.

As it will be developed in that section, the absorption image and KES image are combinations of raw images. In that section we derive the expression of absorption contrast C_{ABS} and noise standard deviation σ_{ABS} as well as KES contrast C_{KES} and standard deviation σ_{KES} from the mean and the standard deviation of count levels of acquired images.

For both modality, raw data consists of an image I_0^Ω taken without the sample, and a sample image containing a set I_A^Ω of pixels filled with material A and a set I_B^Ω of pixels filled with material B. The input flux on the detector at a given energy E will be denoted $I_0(E)$. Assuming no origins of dispersion other than random noise, the image without sample is flat with a mean counts given by

$$\overline{I_0^\Omega} = \int_{\Omega} I_0(E) dE \quad (3.3)$$

for the image with the sample, the mean count is

$$\overline{I_m^\Omega} = \int_{\Omega} I_0(E) e^{-A_m(E)} dE \quad (3.4)$$

for pixels of a sample image filled with material $m \in \{A, B\}$. Here $A_m(E)$ refer to the absorbance of material m and is given by :

$$A_m(E) = \frac{4\pi E l_m}{hc} \Im(n_m(E)) \quad (3.5)$$

Where $\Im(n_m(E))$ is the imaginary part of the refractive index $n_m(E)$ at energy E for material m with density ρ_m and thickness l_m h is the Planck constant and c is the speed of light. The refractive index $n_m(E)$ is taken from xraylib database [20], which gives data with 1 keV spectral resolution.

As in practice the flat image is an image acquired with high statistics in order to correct for systematic dispersion of the gray levels, dispersion of values on flat image will be assumed negligible in comparison with the one of sample image, which standard deviation will be noted σ_m^Ω , evaluated in I_m^Ω .

Let start by establishing the expression of the contrast and noise for absorption modality. The absorption image is typically obtained by dividing the sample image with the flat image. The absorption, gathering counts obtained with both registers of Pixie detector, counting over Ω_1 and Ω_2 respectively, will be expressed by

$$ABS_m = \frac{I_m^{\Omega_1} + I_m^{\Omega_2}}{I_0^{\Omega_1} + I_0^{\Omega_2}} \quad (3.6)$$

Note that as pixieIII is a photon counting detector, with energy discriminating thresholds, images without X-Rays are perfectly darks, so there is no need to correct from any dark levels as it may

usually be done with charge integrating detectors. The mean may be obtained by Taylor expansion [21] of a bivariate function for the ratio function, to give :

$$\langle ABS_m \rangle = \frac{\overline{I_m^{\Omega_1}} + \overline{I_m^{\Omega_2}}}{\overline{I_0^{\Omega_1}} + \overline{I_0^{\Omega_2}}} \quad (3.7)$$

as $\frac{\text{Var}(I_0^{\Omega_1} + I_0^{\Omega_2})}{\langle I_0^{\Omega_1} + I_0^{\Omega_2} \rangle^2} \ll 1$ by assumption, where $\text{Var}(X)$ denotes the variance of the statistical variable X .

Similarly, assuming $\frac{\text{Var}(I_m^{\Omega_1} + I_m^{\Omega_2})}{\langle I_m^{\Omega_1} + I_m^{\Omega_2} \rangle} \ll \frac{\text{Var}(I_0^{\Omega_1} + I_0^{\Omega_2})}{\langle I_0^{\Omega_1} + I_0^{\Omega_2} \rangle}$ (low noise in flats compared to sample images), allows expressing the associated variance as:

$$\text{Var}(ABS_m) = \frac{(\sigma_m^{\Omega_1})^2 + (\sigma_m^{\Omega_2})^2}{(\overline{I_0^{\Omega_1}} + \overline{I_0^{\Omega_2}})^2} \quad (3.8)$$

Then, the CNR for absorption modality is computed as:

$$CNR_{ABS} = \frac{|\langle ABS_A \rangle - \langle ABS_B \rangle|}{\sigma_{ABS}} \quad (3.9)$$

where $\sigma_{ABS} = 0.5 \times (\sqrt{\text{Var}(ABS_A)} + \sqrt{\text{Var}(ABS_B)})$ is the mean of standard deviation of absorption image computed between pixels filled with materials A and B respectively.

KES image may be defined as

$$KES_m = \log \frac{I_m^{\Omega_2}}{I_0^{\Omega_2}} - \log \frac{I_m^{\Omega_1}}{I_0^{\Omega_1}} \quad (3.10)$$

Following similar assumption than the ones used to obtain equations 3.7 and 3.8, one obtains:

$$\left\langle \frac{I_m^{\Omega_i}}{I_0^{\Omega_i}} \right\rangle = \frac{\overline{I_m^{\Omega_i}}}{\overline{I_0^{\Omega_i}}} \quad (3.11)$$

and

$$\text{Var} \left(\frac{I_m^{\Omega_i}}{I_0^{\Omega_i}} \right) = \frac{(\sigma_m^{\Omega_i})^2}{\overline{I_0^{\Omega_i}}^2} \quad (3.12)$$

where $i=1$ or 2 . Then, using Taylor expansion at first order of the log function [21], one may estimate:

$$\left\langle \log \frac{I_m^{\Omega_i}}{I_0^{\Omega_i}} \right\rangle = \log \frac{\overline{I_m^{\Omega_i}}}{\overline{I_0^{\Omega_i}}} - \frac{\text{Var} \left(\frac{I_m^{\Omega_i}}{I_0^{\Omega_i}} \right)}{2 \cdot \left(\frac{\overline{I_m^{\Omega_i}}}{\overline{I_0^{\Omega_i}}} \right)^2} \quad (3.13)$$

and

$$\text{Var} \left(\log \frac{I_m^{\Omega_i}}{I_0^{\Omega_i}} \right) = \frac{\text{Var} \left(\frac{I_m^{\Omega_i}}{I_0^{\Omega_i}} \right)}{\left(\frac{\overline{I_m^{\Omega_i}}}{\overline{I_0^{\Omega_i}}} \right)^2} - \frac{\text{Var} \left(\frac{I_m^{\Omega_i}}{I_0^{\Omega_i}} \right)^2}{4 \cdot \left(\frac{\overline{I_m^{\Omega_i}}}{\overline{I_0^{\Omega_i}}} \right)^4} \quad (3.14)$$

this lead to

$$\langle KES_m \rangle = \left\langle \log \frac{I_m^{\Omega_2}}{I_0^{\Omega_2}} \right\rangle - \left\langle \log \frac{I_m^{\Omega_1}}{I_0^{\Omega_1}} \right\rangle \quad (3.15)$$

and

$$\text{Var}(KES_m) = \text{Var} \left(\log \frac{I_m^{\Omega_2}}{I_0^{\Omega_2}} \right) + \text{Var} \left(\log \frac{I_m^{\Omega_1}}{I_0^{\Omega_1}} \right) \quad (3.16)$$

Thus, the CNR for KES modality may be expressed as:

$$CNR_{KES} = \frac{|\langle KES_A \rangle - \langle KES_B \rangle|}{\sigma_{KES}} \quad (3.17)$$

where $\sigma_{KES} = 0.5 \cdot (\sqrt{\text{Var}(KES_A)} + \sqrt{\text{Var}(KES_B)})$.

Equation 3.9 and 3.17 give expression of CNR computed from input spectrum $I_0(E)$, gray level $I_m^{\Omega_i}$ for both material and noise $\sigma_m^{\Omega_i}$ on raw data. The remaining of that section is dedicated to describe models for these quantities.

3.2 Source model

In the above expression, one needs to evaluate $I_0(E)$ over the considered energy ranges. There are basically two possibilities for that: using simulated spectrum or an empiric one. We used SpekPy([22, 23]) to simulate the input spectrum that illuminates the sample. This model simulates tungsten anode reflection sources, at desired voltage and current and any source-detector distances.

Alternatively, we can also obtain an input spectrum by doing a threshold scan with Pixie-III (i.e., acquiring flat images with increasing threshold value and then differentiating successive images to obtain a spectrum).

3.3 Absorption model

In order to evaluate the terms $\overline{I_m^{\Omega_i}}$, one needs evaluations of the absorbance spectra $A_m(E)$ for any E . As described in the last section, this is basically done using xraylib. However, due to finite resolution of the detector, the measured K-edges are smoother than the tabulated values. In order to take into account that effect, we measure absorbance spectra with the phantom sample described in section 2. Images with and without the phantom were acquired with the detector using the low register only with E_L varying from 15 to 50 keV by steps of 1 keV. The mean number of count per pixel for images without the sample ranges from 20 000 for $E_L=15\text{keV}$ to 500 for $E_L = 40 \text{ keV}$. Then, successive images were differentiated to obtain the number of counts per energy bins of 1 keV width. For each energy bins, the image with the sample was divided by the image without, and the opposite of the logarithm of the result was computed to obtain spectral image series of the absorbance. For each of the three tube, a mean spectrum was computed as the mean value over an ROI consisting of a column of pixel centred in the centre of the tube so that the thickness of solution correspond to the tubes' diameter. Finally, the spectrum obtained from the water tube was subtracted from those obtained from the Iodine and Barium tubes in order to remove contributions from the glass tube and water. This results in the absorbance spectra $A_{KI}(E)$ and $A_{BaSO_4}(E)$ of iodine and barium sulfate respectively. The obtained spectra are the light blue solid curves in figure 3. The tabulated spectra obtained using xraylib are displayed in orange dashed line. As one can

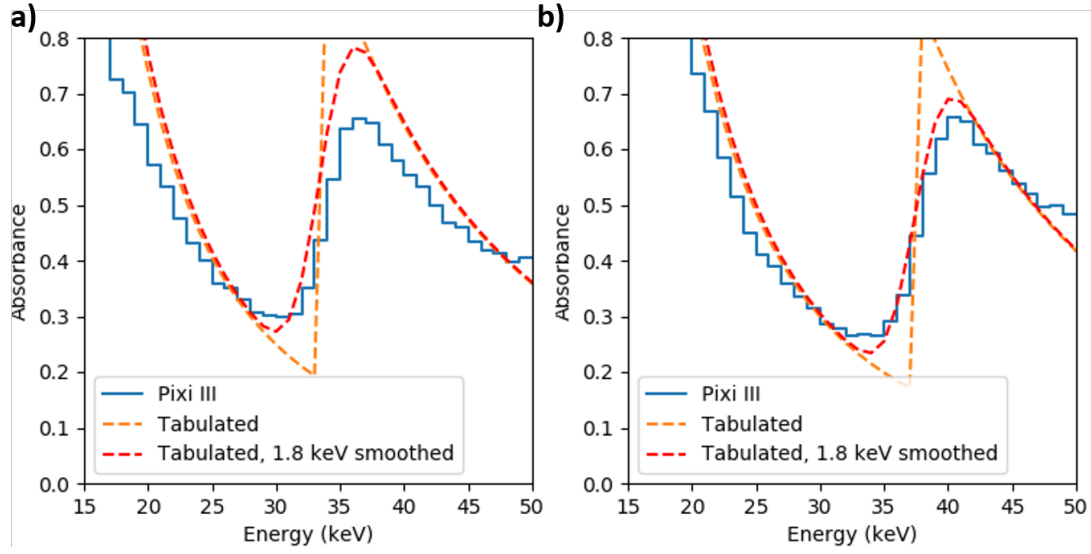


Figure 3. Absorbance spectra for Iodine and BaSO_4 solution measured with PixiRad-2/PixieIII (solid blue curve) compared against computed ones from tabulated value of refractive index (orange dashed line), and computed one with Gaussian kernel of 1.8 keV (red dashed line). a) For iodine and b) for barium solution

see, the position of the K-edge measured by the detector is correct, as well as the global evolution of the absorbance. However, one needs to account for the spectral resolution of the detector, which is necessarily finite and leads to a smoothing of the edges, which is then not measured as a strict vertical edge. This is done by applying a Gaussian smoothing with a 1.8 keV kernel. This value was chosen in order to reproduce the experimental slope of the edge. The result is represented by the red dashed line in figure 3. As one can see, the resulting spectra are really close to the measured one. In the model, smoothed values of $A_m(E)$ (eq. 3.5) are used to compute $\overline{I_m^{\Omega_i}}$ terms.

3.4 Noise model

The last part of the model is the prediction of the standard deviation $\sigma_m^{\Omega_i}$ that one can expect on the acquired images.

As mentioned in the introduction, previous papers ([14–16]) focused on modelling Poisson noise from the source. Here we aimed at studying noise arising from the acquisition procedure. Particularly, we focus on the dependence of the noise on threshold values. To that purpose, we acquired a set of images without sample, taking all possible combinations of thresholds, between 25 keV and 46 keV by step of 1 keV and using the low energy register, i.e. counting photons in the range $[E_L, E_H]$. For each combination of threshold, 50 images of 1s of exposure time were taken.

Then we processed the data as follows: for each combination of thresholds, a flat field corrected image was obtained by dividing the first image of the series of 50 images by the median of these 50 images, and the resulting image is then multiplied by the mean value of the median image. This correction permits to compensate the dispersion of the gray values arising from the inhomogeneity of the beam, and pixel to pixel systematic variations, leaving noise as the remaining source of

dispersion of the gray values, so that the image fit the assumptions of the model described in section 3.1

Pixel with a zero value in the median image were labelled as defective. Then, for each combination of thresholds, mean count level I and standard deviation σ were computed on a ROI of 1850 pixels (370x5) of the flat-field corrected image, ignoring defective pixels. Figure 4 shows

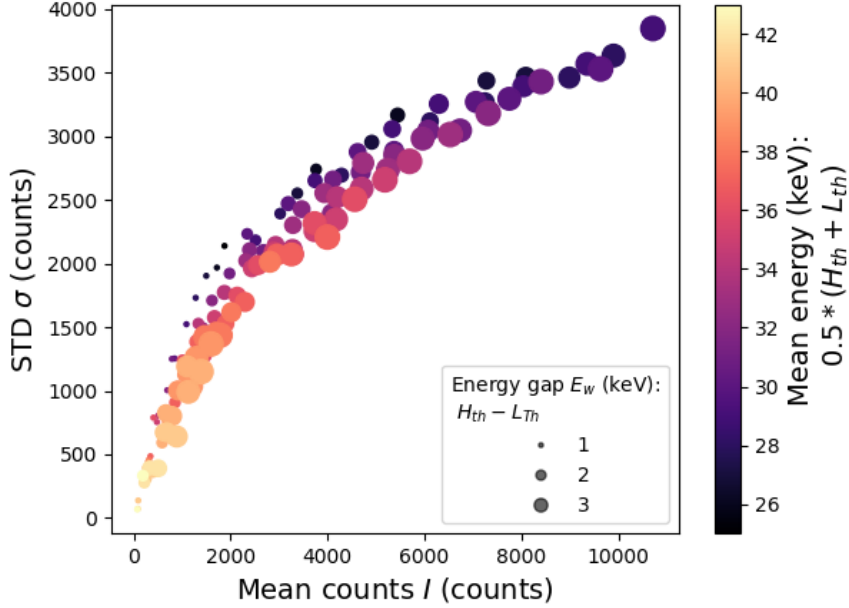


Figure 4. Evolution of standard deviation with mean counts. Colour refers to the mean of the two energy thresholds and size of dots to the difference of the two energy thresholds.

the variation of the relation between mean count level and standard deviation when varying mean energy $E_{mean} = 0.5 * (E_L + E_H)$ and energy bin width $E_w = E_H - E_L$. As one may see, the relation between noise and input flux is dependent on the values of the thresholds. In order to investigate that dependence, we modelled the measured noise as being the beam intrinsic σ_{intr} (proportional to the square root of the input flux) noise affected by a prefactor Γ that may depend on the thresholds values and possibly flux:

$$\sigma = \sigma_{intr} \cdot \Gamma(E_{mean}, E_{gap}, I) \quad (3.18)$$

Representing the intrinsic noise by $\sigma_{intr} = \sqrt{I}$ (thus letting the proportionality factor in the prefactor) permits to compute the prefactor with:

$$\Gamma = \frac{\sigma}{\sqrt{I}} \quad (3.19)$$

This quantity is represented in figure 5, as a function of I , for three value of E_w , and colour corresponding to E_m . One can see a first dependence of σ with I and/or E_{mean} : σ increases with I while E_{mean} decreases. However, as the experiment is performed without filter on the source, it is expected that the mean count decreases with the bin mean energy. Additionally, a clear dependence can be observed on E_w : points of different size appear to align along different curves. We suppose

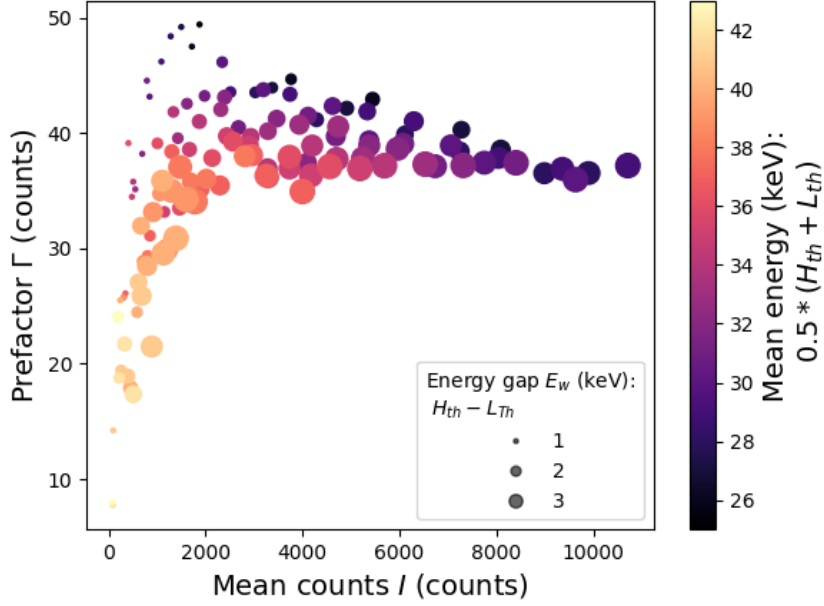


Figure 5. Evolution of the prefactor computed with 3.19 with mean counts. Colour refers to the mean of the two energy thresholds and size of dots to the difference of the two energy thresholds.

that this effect might be due to finite spectral resolution of the detector: Ideally, when a photon interact with the detector, it should be counted if and only if its energy lies in the energy bin defined by threshold values, i.e. the evolution of the probability for a photon to be counted presents a jump from 0 to 1 at the thresholds values. However, in practice, that probability evolves smoothly over a finite energy range centred on the thresholds values. As a result, some photons with an energy lying in that transition range may be badly counted. This results in an additional noise which increases with decreasing the bin width, as the proportion of badly classified photons increases (since the mean difference between photons energies and threshold value decreases).

In order to parametrize that dependence, the left panel of figure 6.a) present the evolution of the prefactor against mean count I for different fixed E_w (dots). From the evolution, to describe the relation between prefactor Γ , E_w and I we propose a function of the form:

$$\Gamma(E_w, I) = B(E_w)(1 - e^{-\frac{I}{I_c(E_w)}}) \quad (3.20)$$

where B and I_c are fitting parameters (amplitude and characteristic Intensity) that depends on the bin width E_w . This shape has been fitted on the data point using least square optimization (solid curves on left panel) and the evolution of the fitting parameters B , and I_c against E_w are displayed on panels b) and c) of the figure. Evolution for B is monotonically decreasing. I_c is approximately increasing up to a given value then does not evolve. In fact, from left panel, one see that for largest bin width, the prefactor depends on I only for really low count rate. Thus, we suggest parametrizing those evolutions with a decreasing exponential shape for B and a piecewise constant function for

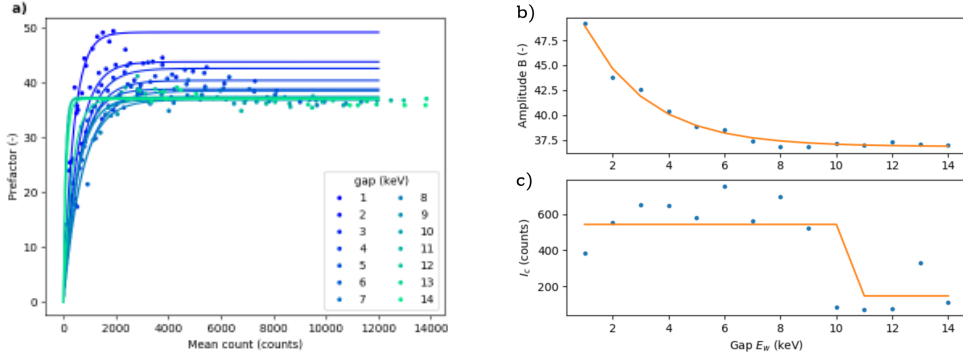


Figure 6. a) evolution of prefactor with mean count level for different bin with I (dots), and fitted model from eq. 3.20. b) and c) evolution of the fitting parameter amplitude B and characteristic intensity I_c of this model with E_w (dots), and fitted parametrization given in eq 3.21 (orange solid line).

I_c . Least square fitting of these shapes gives:

$$B(I) = 36.9 + 18.8e^{-E_w/2.28}$$

$$I_c(I) = \begin{cases} 544 & \text{if } E_w \leq 10\text{keV} \\ 147 & \text{else} \end{cases} \quad (3.21)$$

for E_w in keV.

As a summary, equations 3.18, 3.20 and 3.21 forms a model to estimates the noise σ from the mean count on detector I , and the detectors thresholds, or more precisely, the energy bin width E_w .

We check the goodness of fit of the parametrization by plotting the estimated standard deviation from I and E_w against the measured one in figure 7. On this figure, one can see that the point align along the dashed line which the $y = x$ line. It means that the developed parametrization succeed in explaining the variability of the dataset.

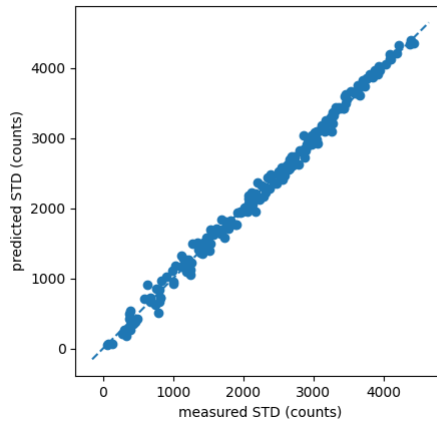


Figure 7. Validation of the model: estimated standard deviation compared against measured standard deviation from dataset.

4 Results

4.1 Resolution

Now we get an expression for estimating contrast and noise from experimental configuration parameters, we need to specify the procedure to find the optimum and the associated constraints.

The procedure is detailed by algorithm 1. As a first implementation, the principle is exhaustive, i.e. it is to evaluate CNR at all points of discrete search ranges Ω_U (for voltage), Ω_{E_L} (for E_L) and Ω_{E_H} (for E_H). Optionally, during the computation of CNR, the current is set so that a prescribed count level CL is obtained on the detector when the sample is out of the beam for each set of voltage and thresholds. Then, raw images mean counts $\overline{I_m^{\Omega_i}}$ and $\overline{I_0^{\Omega_i}}$, and noise and raw images $\sigma_m^{\Omega_i}$ are

Algorithm 1 Algorithm to optimize $(U, E_L, E_H, \text{mode}, i)$ for maximum CNR

for all $(U, E_L, E_H) \in \Omega_U \times \Omega_{E_L} \times \Omega_{E_H}$ **do**

Optionally, compute source spectrum $I_0(E) \forall E \in [0, U]$ for a seed current i_s

Compute current to reach desired count level CL on registers: $i(U, E_L, E_H) = \frac{CL}{\max(I_0^{\Omega_1}, I_0^{\Omega_2})} \cdot i_s$

Estimate mean gray level on raw images $\overline{I_m^{\Omega_1}}, \overline{I_m^{\Omega_2}}, \overline{I_0^{\Omega_1}}, \overline{I_0^{\Omega_2}}$

Estimate noise on raw images $\sigma_m^{\Omega_1}$ and $\sigma_m^{\Omega_2}$ using equations 3.18 3.21

Compute absorption CNR using eq 3.9

Compute KES CNR using equation 3.17

end for

Find optimum $(U_{opt}, E_{L,opt}, E_{H,opt})$, mode and current $i(U_{opt}, E_{L,opt}, E_{H,opt})$ for highest CNR.

estimated. From these variables, CNR for both absorption and KES modality are computed. Once these computations for all combinations of source voltage, and detector thresholds are performed, the best configuration is extracted by searching for the maximum CNR obtained.

4.2 Validation

In order to evaluate the model, we compared predictions in terms of voltage and thresholds to empirical optimization performed on a test sample by evaluating K-Edge CNR for all combination of thresholds in given ranges. The dataset was obtained using the phantom sample used described in section 2. This sample allows testing model on three contrast : and I/BaSO₄, water/BaSO₄, water/KI. For that acquisition, the source was operated with 50 kV acceleration voltage, a target current of 14μA, exposing for 1s at an SDD = 281.12 mm, and SOD = 25.08 mm, thresholds varying from 25 to 45 keV by step of 1keV. For each couple of low and high thresholds within that range and for each energy bin, 50 beam images were acquired and 2 images of the sample were taken. The images were averaged in order to get one beam image and one sample image per couple of thresholds from which KES images were computed.

Then, CNR was computed from mean count level and standard deviation measured over ROIs focusing on each material. The ROIs were made of 3600 pixels (360x10) centred on their corresponding tubes. While this implies a heterogeneous thickness of tube traversed by the X-rays, it is necessary to get sufficient statistics. In parallel, the simulation of that problem was performed

using the model presented in the previous section. As the model is made from different sub-models, let us first compare some intermediate variables to evaluate these different sub-models. The top row of figure 8 compares $\overline{I_{KI}^{\Omega_1}}$, the mean gray level on the ROI focusing on KI tube measured on the low energy register; bottom: $\sigma_{KI}^{\Omega_1}$, the standard deviation measured on that same ROI and low energy register. We can see that for both variables, simulated values are close to the experimentally

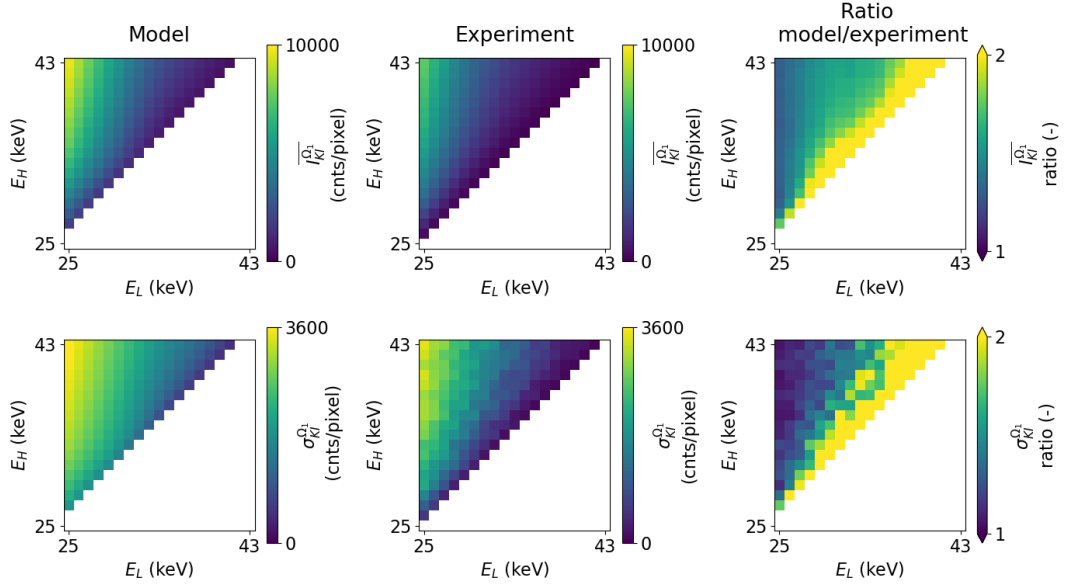


Figure 8. Comparison of intermediates variable as function of the two energy thresholds. Top row: $\overline{I_{KI}^{\Omega_1}}$, bottom row: $\sigma_{KI}^{\Omega_1}$. Left column: simulated quantities, middle column: experimental quantities, right column: ratio between simulated and experimental.

measured ones (last 2 figures of figure 8). The shapes of the maps of these variables are respected, and quantitatively, the value are globally well respected, particularly where E_w and the number of counts are highest. For E_w getting close to 1, the error increases and the ratio of simulated values over experimental one is globally about 5-6.

Then we compare KES CNR maps with respect to the two threshold values (see figure 9). Optimal configuration were then defined as the maximum of these CNR maps. The empirical optimum is represented by the red dot and the simulated one by the red cross. Additionally, we represent the value of the corresponding K-edges by grey dashed lines.

Let's begin the comparison with the top row, i.e. for BaSO₄/KI contrast. The general shape of the modelled map is close to the experimental one. From top right to bottom left: CNR is low for any configuration with both threshold above both K-edges, a principal maximum is reached for low thresholds between both k-edges, and high threshold above Ba K-edge. A secondary maximum at the bottom left part of the map where both thresholds are below both K-edges and a narrow "valley" of minima separate both maximum. Keeping in memory that KES signal measures the variation in absorption between the two energy bins, the principal maximum corresponds to the Ba K-edge as this implies strong variation for BaSO₄ while moderate ones for KI. The secondary maximum can be understood by seeing the KES CNR as the difference of absorption CNR between the two

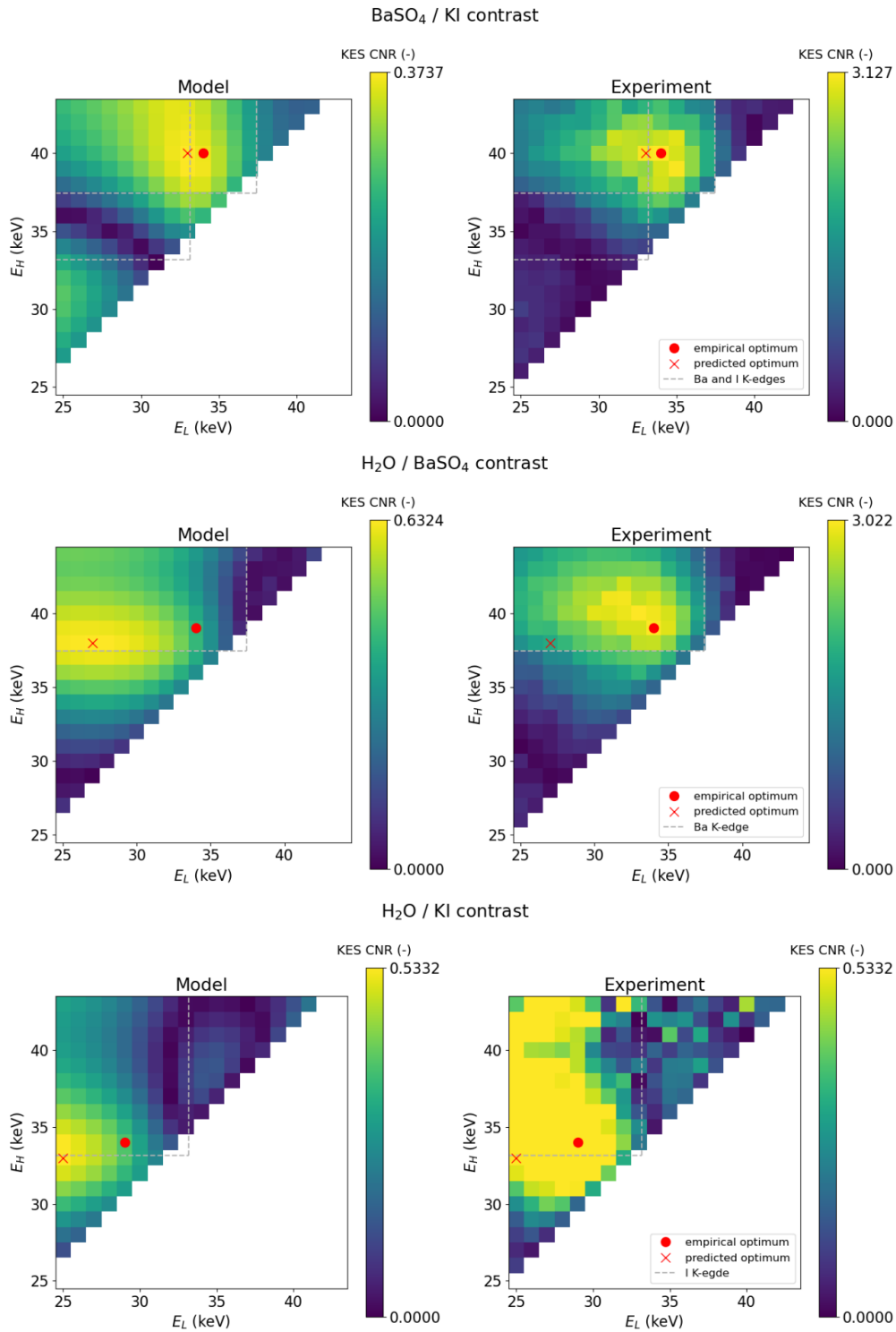


Figure 9. Comparison of simulated (left column) and experimental (right column) CNR maps for K-edge modality obtained with BaSO₄ / KI / water test phantom: BaSO₄/ KI contrast (first row), water/ BaSO₄ contrast (second row) and water/KI (third row)

energy bin. This maximum corresponds to a configuration where the high energy bin includes both K-edges so that the absorption CNR between both material on that energy bin is low. It remains that the KES CNR in that configuration is made only from the absorption CNR on the lower energy bin which focus on the monotonically decreasing part of the spectra. The minimum between these maxima corresponds to a configuration where the lower energy bin is centred on the lower K-edge and the higher energy bin on the highest K-edges. In that configuration, contrast vanishes as for each bin absorption is stronger for one material on the first part of the bin, and stronger for the second material in the second part of the bin so that absorption CNR is low on both energy bin. Quantitatively, the model predicts an optimum at (33 keV, 40 keV) with a CNR of 0.4 while the empirical optimum is (34 keV, 40 keV) with a CNR of 3.1. The secondary maximum for model and experiment is respectively about 0.3 and 0.4.

Maps for BaSO₄/water or KI/water CNR exhibit simpler shapes as the K-edge split the map in 3 area: Both maxima are reached with low thresholds clearly below the K-edge and high threshold at the K-edge value and CNR get low values and even vanishes if both thresholds are above (upper right part) or below (bottom left part) the K-edge. Quantitatively, for BaSO₄/water contrast, the model predicts an optimum at (27 keV, 38 keV) with a CNR of 0.6 where it is (34 keV, 39 keV) with a CNR of 3.0 for the experiment. For KI/water contrast, the model predicts an optimum at (25 keV, 33 keV) with a CNR of 0.5 where it is (29 keV, 34 keV) with a CNR of 0.9 for the experiment. The quantitative differences between model and experiment described in that section will be commented in section 5.

For a qualitative appreciation of these results, figure 10 shows images obtained a) with conventional approach, using the images from the high energy register with $E_H = 26$ keV (1 phantom images and 50 flat images for flat field correction) b) KES image obtained by procedure described above at the predicted optimum for BaSO₄/KI contrast, i.e. $E_L=33$ keV, $E_H=40$ keV, c) KES image at empirical optimum for BaSO₄/KI contrast, i.e. $E_L=34$ keV, $E_H=40$ keV, d) KES image at the predicted optimum for BaSO₄/water contrast, i.e. $E_L=27$ keV, $E_H=38$ keV and e) KES image at the empirical optimum for BaSO₄/water contrast, i.e. $E_L=34$ keV, $E_H=39$ keV Two observations can be made: i) KES imaging permits to considerably increase the contrast between KI and BaSO₄, even removing water and glass capillary tubes from the image, and ii) KES images obtained at predicted and empirical optima are visually very close.

4.3 Application example

In order to illustrate the application of the model, we show here optimization results with BaSO₄ and KI, fixing density of BaSO₄ and varying density of KI.

The materials whose contrast has to be optimized are 1 mm of BaSO₄ at 0.46g/cm³, and 1 mm of KI at density in range [0.1g/cm³, 0.5g/cm³]. For each density of KI, algorithm 1 is applied with $\Omega_U = [50,80,100]$, $\Omega_{E_L} = \Omega_{E_H} = [[25 \text{ keV}, 45 \text{ keV}]]$ and $CL = 10000$. Figure 11 shows the evolution of the absorption and KES CNR computed from equations 3.9 and 3.17 respectively. As one may see, the modality to obtain the highest CNR is not necessarily KES depending on the concentration of the materials. KES is recommended for density of iodine in range [0.24 g/cm³, 0.37 g/cm³] and absorption is recommended elsewhere. The curve for absorption can be split in two parts: a first decreasing and a second increasing with iodine density. The plots a) to d) of figure 12 display the optimal choice of thresholds for both modality (represented by vertical dashed

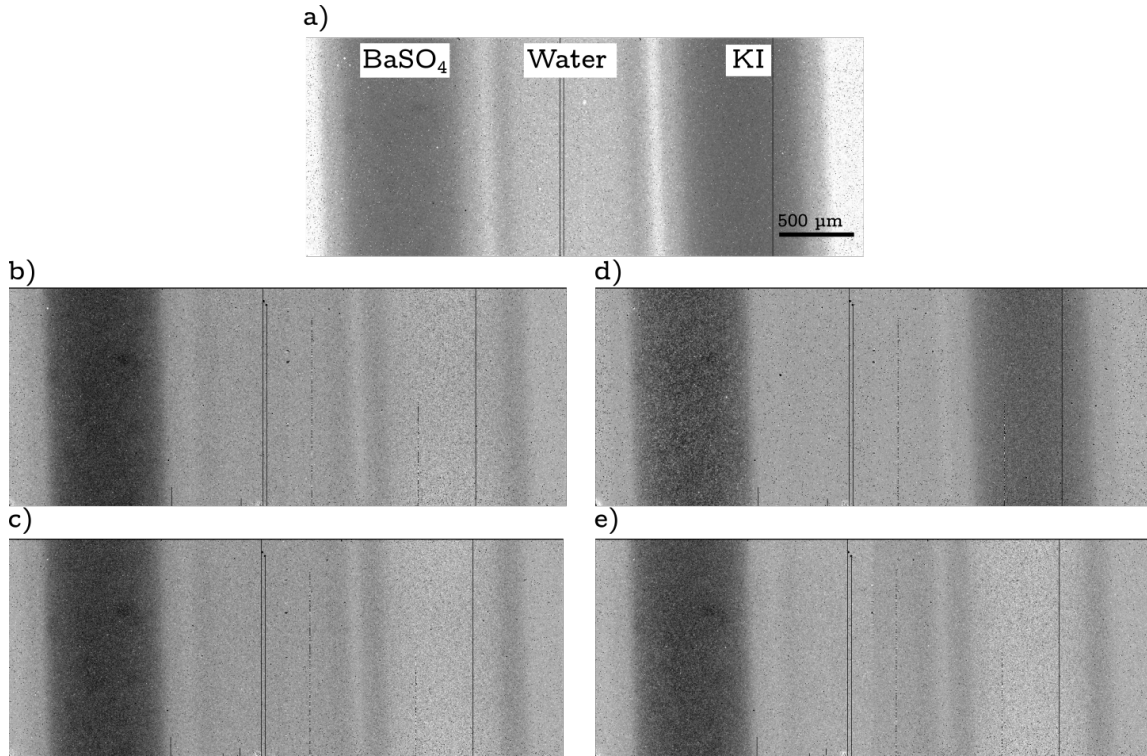


Figure 10. Comparison of the phantom images with a) simple absorption (high energy bin, $E_H = 26$ keV, b) KES images, modelled optima or BaSO₄/KI contrast ($E_L=33$ keV, $E_H=40$ keV) and c) KES images at empirical optima for BaSO₄/KI contrast ($E_L=34$ keV, $E_H=40$ keV) c) KES images at modelled optima for BaSO₄/water contrast ($E_L=27$ keV, $E_H=38$ keV) d) KES images at empirical optima for BaSO₄/water contrast ($E_L=34$ keV, $E_H=39$ keV). Dark vertical lines are columns of defective pixels, ignored in the measurements of quantities related to gray level.

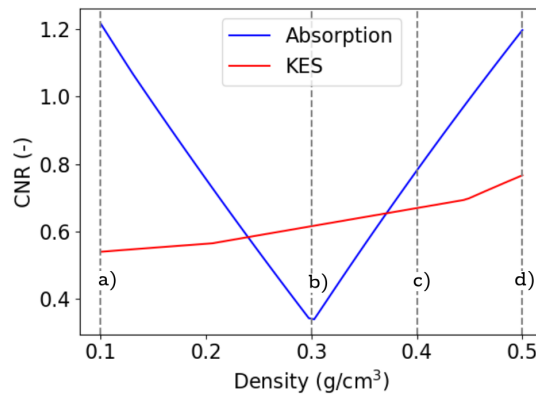


Figure 11. Evolution of optimal absorption and KES CNR between BaSO₄ and KI as function of KI density for BaSO₄ density fixed at 0.46 g/cm³. Letters correspond to the different panels of figure 12, plotting absorbance spectra at difference densities represented by the gray dashed vertical lines.

lines: blue for absorption and red for KES) in relation with the absorbance spectra of the two material (solid curves: orange for barium, green for iodine) as well as the optimal voltage (black solid vertical line) which was found to be 50kV for all configurations.

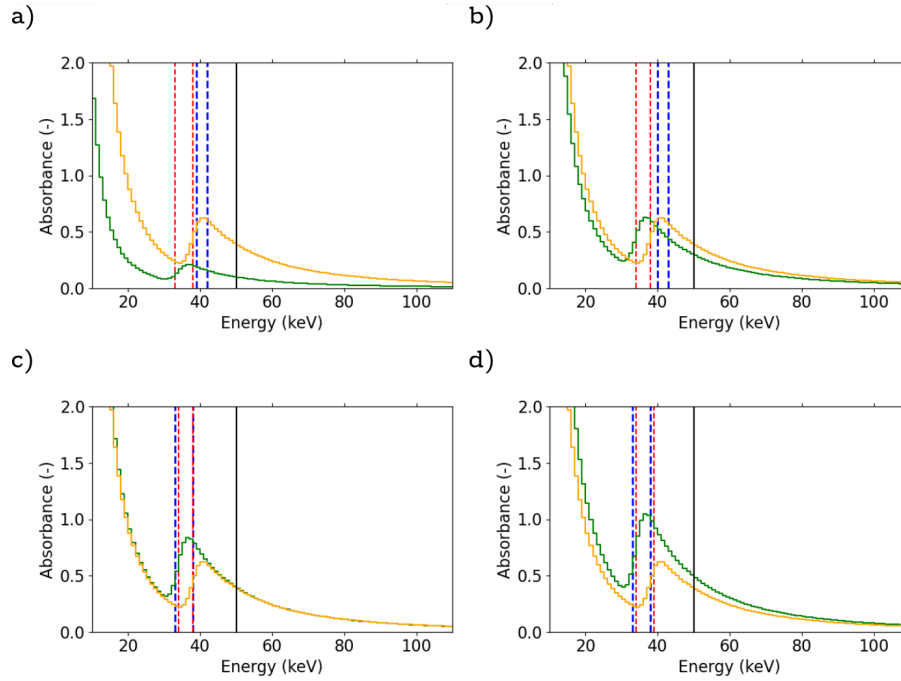


Figure 12. Plot of absorbance spectra of both material at different characteristic densities of iodine, corresponding to vertical gray dashed lines on top figure: a) $0.1\text{g}/\text{cm}^3$, b) $0.3\text{g}/\text{cm}^3$ c) $0.4\text{ g}/\text{cm}^3$ d) $0.5\text{ g}/\text{cm}^3$. Blue and red vertical dashed lines represent the optimal thresholds for absorption and KES modality respectively at the corresponding density. The vertical dark solid line represents the highest photon energy in the source spectrum with voltage at 50kV, the optimal voltage.

Let us focus on the absorption first: blue solid curve on figure 11, and blue dashed line on figure 12. For low KI density, BaSO_4 has the highest contrast, and the difference is at its highest above Ba K-edge, the strategy for point a) and b) is then to focus on that part of the spectrum ($E_L \approx 40\text{keV}$) and choosing the high threshold so both detector count as much as they can (i.e. E_H is set so that CL is reached on both detectors). As the iodine density increases, the spectral contrast above the Ba K-edge reduces and gets inverted (iodine more absorbent than barium) between the two K-edges. This explains why the absorption CNR decreases with iodine density up to $0.3\text{ g}/\text{cm}^3$. At this point, the best strategy for absorption modality becomes to focus on the part of the energy domain where KI is the most absorbent. Then, the thresholds are set so that the low energy bin focus on the part where iodine is the most absorbent. From here, since the CNR is built from the fact that KI is the most absorbent, the absorption CNR keeps increasing with KI density. Now focus on the KES modality: red solid curve on top panel, and red dashed line on a)-d) panels.

The strategy for KES is to focus the low energy bin on the part between both K-edges, and the high energy bin above the Ba K-edge. One may notice that the curve for KES CNR is much flatter than for absorption, this may be an interesting fact to ensure an acceptable CNR for example sample containing areas with variable density of KI or unknown composition.

Thus, this example illustrates how the present model permits to take into consideration different strategies and put them into balance.

5 Discussion

First, it has to be precised that the version of the PixiRad2-PixieIII we own exhibits a salt and pepper noise when used in NPISUM (see figure 10) mode. This artefact is not a normal behaviour of the detector, but is known to be linked to errors showing up randomly in the 15bit counters of the detector. A first consequence of this, is that the current noise level is particularly high and globally the CNR values described above somewhat underestimate the performances the technology has to offer. In the future, this extra noise is brought to disappear with the resolution of this issue, thus the noise model will need to be updated. However, the current dependencies described by that model (on the mean count level and E_w for the low energy register) are explained on the basis of other phenomenons intrinsic to the detector technology. Thus, we may expect that the current shape of the noise model is not affected by this artefact. Without that noise artefact, one may need to re-adjust the parameters of the parametrization by reproducing the exposed experiment, seeing it as a calibration procedure of the current model.

The presented model allows reproducing qualitatively well the variations of CNR with energy thresholds of the detector. Particularly, the shapes of the maps on figure 9 are correct, and the predicted optimum is quantitatively correct for the case where KES imaging is the most relevant. However, noticeable errors remain. Both flux and noise standard deviation on detector after going through the materials shows increased error for small energy bins (i.e. for E_H and E_L close). As the mean intensity is used by the noise model to estimate the noise standard deviation, it is expected that the error seen in $\overline{I_m^{\Omega_i}}$ propagates in $\sigma_m^{\Omega_i}$ and at the end in the computed CNR. The errors seen on $\overline{I_m^{\Omega_i}}$ originates from the input flux model $I_0^{\Omega_i}(E)$ and sample absorbance model $A_m(E)$. Additionally, the CNR computed in the 4.2 appeared underestimated up to a factor $\simeq 10$ for KI/BaSO₄ contrast. This quantitative errors may have several explanations:

- The exposed results demonstrate the performances when used without prior empirical knowledge of the other elements from the imagery chain, i.e. this demonstrates the minimal performance of the model. The results may be improved if one dispose of i) empirical source spectra $I_0^{\Omega_i}(E)$ ii) empirical absorbance spectrum of the samples $A_m(E)$. Both these spectra may be measured using Pixie-III by performing a threshold scan.
- Secondly, as it has been shown in section 3.4, the noise depend on both input flux and thresholds, i.e. it shows a spectral sensibility. However, although the developed noise model fits well to the data for images without the sample, the terms $\sigma_m^{\Omega_i}$ are computed taking into account the effect of the sample on the input flux only, but not on the spectrum shape. Thus, it may happen that the parametrization does not give accurate estimations for those terms, particularly when E_w is small. This would be a point to be studied in finer details.
- The ratio $\frac{\overline{I_m^{\Omega_i}}}{\sigma_m^{\Omega_i}}$ ranges from 1 to 5 in the validation example, and is about 1.2 for the coordinates of the optimum. Additionally, the specific salt and pepper noise described at the beginning of that section is made of values far from the mean. For both reasons, the presented Taylor

expansions may not hold. For example, experimentally, in eq. 3.14, the first order term (second term in the right-hand side) represents 0.17 times the zero order term, which is not completely negligible yet.

From figure 9, particularly for BaSO₄ contrast, one can see that the model predicts a wider low energy bin than found experimentally (lower E_L). Taking into account efficiency of the detector may improve that aspect. Indeed, at the moment, the input flux model does not take into account detector specificities : typically efficiency and linearity. It is anticipated that efficiency decreases significantly for energy above the Cd and Te K-edges (26.7 keV and 31.8 keV respectively) since part of the incoming photons leads to fluorescence. The bin width results from a trade-off between KES signal and statistics. Thus, in practice, energies just below the K-edges are under-weighted in the measurement of the absorbance on the low energy bin in comparison to the lowest energies of that bin. The absorbance measured on that bin is then larger than expected (as spectral absorbance is monotonically decreasing below the K-edge) and thus the KES signal is reduced. As a consequence, this pushes to take narrower low energy bin in order to compensate that loss of KES signal. The optimum is then moved towards higher E_L value. This effect should increase with the K-edge energy of the sample as the efficiency decreases, this is actually the case when comparing KI/water contrast to BaSO₄ contrast. Additionally, this effect is not observable for the KI/BaSO₄ as in that case the trade-off is to not mix KES signal from both K-edges as they would annihilate each other. In that case, both model and experiment results in taking E_L just above the lower K-edge.

Finally, the optimization procedure described by algorithm 1 is quite simple. One may consider developing it into a refined procedure by adding some constrains on the product exposure time times source current intensity. Indeed, when asking a count level CL in the image, the algorithm adapt that product to reach that level. In practice both parameters are limited. The source is physically limited by the design of the source and the exposure time is in practice limited to get a reasonable acquisition time or by the need in time resolution for in-situ experiment for example. Additionally, one may include additional modalities in the comparison. For example, it would be straightforward to consider the absorption image obtained uniquely on the low energy bin. This would consider an absorption modality where some low and high energies are ignored. This may be interesting for a case like the one depicted in figure 12.b where the contrast is mainly due to the absorption difference in the low energy bin, but the high energy image is contrasted in the opposite manner and finally reduces the global contrast if summing the counts from both energy bins.

6 Conclusions and perspectives

We designed a model that estimates CNR of both absorption and KES modalities for Pixie-III photon counting detector. The model optimizes the setup parameters : voltage U, the product exposure time times intensity, thresholds E_L and E_H and acquisition modality (conventional absorption or KES). The model can be broken down into sub-models that can be used and improved independently. Particularly, we have presented:

- A noise model, that evaluate the standard deviation of count levels on a representative ROI of homogeneous material. Besides accounting for intrinsic Poisson noise which evolves as the square root of the mean intensity, the noise model includes an empirical parametrization

of Pixie-III that reveals and takes into account a specific behaviour of the detector for small bin width E_w . The resulting parametrization reproduces quantitatively the data.

- A noise propagation model that evaluate CNRs for absorption and KES modalities on the projection image at the end of the processing chain.

Computationally speaking, the model reduces to simple operations on spectral integrals which lead to instantaneous computations. The optimization consists in an exhaustive exploration of the space of acquisition parameters given a desired count level on the images. The output typically consists of maps of CNR in the space of acquisition parameters. Confrontation with experimental exploration of the parameters shows that the model reproduces well the shapes of the maps. The prediction in terms of thresholds compares within few keV with experimental. Globally, the model tends to predict lower threshold values than the ones suggested by experiment. Quantitatively, the error tends to increase with small energy bins. Additionally, it has to be kept in mind that the detector currently in our possession suffer from a random noise artefact. That should not impact the predicted optimal parameters, but may require recalibration of the noise model for quantitative predictions. Finally, it has been illustrated how the model enables to compare different strategies to enhance the contrast and how it allows to understand the underlying trade-offs the operator has to make.

By these developments, this work constitutes a base from which additional improvements may be considered. This includes:

- to push forward the noise model by taking into account the effect of sample on the spectrum of the X-ray beam.
- to account for linearity and efficiency of the detector. Particularly, this would improve the predictions for sample with K-edge above CdTe K-edges.
- to design more advanced resolution algorithms, this includes : additions of derivate modalities in the comparison, constrains on the space of set up parameters, computational improvement of the optimization scheme.

Supplementary Materials

The model as been implemented in Python and is available on gitlab : https://gricad-gitlab.univ-grenoble-alpes.fr/TomoX_SIMaP/px3opt

Acknowledgments

This project was funded by the French National Research Agency ANR-18-CE42-0005. 3SR is part of LabEx Tec 21 - ANR-11-LABX-0030 and of Institut Carnot PolyNat (ANR16-CARN-0025). SIMAP is part of LabEx CEMAM (ANR-10-LABX-44-01).

References

- [1] E. Maire and P. J. Withers, *Quantitative X-ray tomography*, *International Materials Reviews* **59** (Jan., 2014) 1–43.
- [2] K. A. Nugent, T. E. Gureyev, D. F. Cookson, D. Paganin and Z. Barnea, *Quantitative phase imaging using hard x rays*, *Physical review letters* **77** (1996) 2961.
- [3] D. Paganin, *Coherent X-ray Optics*. No. 6. Oxford University Press on Demand, 2006.
- [4] G. R. Myers, S. C. Mayo, T. E. Gureyev, D. M. Paganin and S. W. Wilkins, *Polychromatic cone-beam phase-contrast tomography*, *Physical Review A* **76** (Oct., 2007) 045804.
- [5] W. Thomlinson, *K-edge subtraction synchrotron X-ray imaging in bio-medical research*, *Physica Medica* (2018) 19.
- [6] B. Jacobson, *Dichromatic Absorption Radiography. Dichromography*, *Acta Radiologica* **39** (June, 1953) 437–452.
- [7] B. K. Rutt, I. A. Cunningham and A. Fenster, *Selective iodine imaging using lanthanum K fluorescence*, *Medical Physics* **10** (1983) 801–808.
- [8] Z. Zhong, D. Chapman, R. Menk, J. Richardson, S. Theophanis and W. Thomlinson, *Monochromatic energy-subtraction radiography using a rotating anode source and a bent Laue monochromator*, *Physics in Medicine and Biology* **42** (Sept., 1997) 1751–1762.
- [9] E. Rubenstein, *Medical imaging with synchrotron radiation*, *Nuclear Instruments and Methods in Physics Research* **222** (May, 1984) 302–307.
- [10] H. Elleaume, A. M. Charvet, S. Corde, F. Est ve and J. F. L. Bas, *Performance of computed tomography for contrast agent concentration measurements with monochromatic x-ray beams: Comparison of K-edge versus temporal subtraction*, *Physics in Medicine and Biology* **47** (Sept., 2002) 3369–3385.
- [11] S. Kulpe, M. Dierolf, E. Braig, B. Günther, K. Achterhold, B. Gleich et al., *K-edge subtraction imaging for coronary angiography with a compact synchrotron X-ray source*, *PLOS ONE* **13** (Dec., 2018) e0208446.
- [12] R. Ballabriga, J. Alozy, M. Campbell, E. Frojdh, E. H. M. Heijne, T. Koenig et al., *Review of hybrid pixel detector readout ASICs for spectroscopic X-ray imaging*, *Journal of Instrumentation* **11** (2016) .
- [13] R. Bellazzini, A. Brez, G. Spandre, M. Minuti, M. Pinchera, P. Delogu et al., *PIXIE III: A very large area photon-counting CMOS pixel ASIC for sharp X-ray spectral imaging*, *Journal of Instrumentation* **10** (Jan., 2015) C01032–C01032.
- [14] P. He, B. Wei, W. Cong and G. Wang, *Optimization of K-edge imaging with spectral CT*, *Medical Physics* **39** (Nov., 2012) 6572–6579.
- [15] P. He, B. Wei, P. Feng, M. Chen and D. Mi, *Material Discrimination Based on K-edge Characteristics*, *Computational and Mathematical Methods in Medicine* **2013** (2013) 308520.
- [16] B. Meng, W. Cong, Y. Xi, B. De Man and G. Wang, *Energy Window Optimization for X-ray K-edge Tomographic Imaging*, *IEEE transactions on bio-medical engineering* **63** (Aug., 2016) 1623–1630.
- [17] F. Brun, V. D. Trapani, J. Albers, P. Sacco, D. Dreossi, L. Brombal et al., *Single-shot K-edge subtraction x-ray discrete computed tomography with a polychromatic source and the Pixie-III detector*, *Physics in Medicine & Biology* **65** (Mar., 2020) 055016.

- [18] V. Di Trapani, L. Brombal, S. Donato, B. Golosio, R. Longo, P. Oliva et al., 36. *Optimization of the acquisition threshold of Photon Counting Detectors (PCDs) used in X-ray medical imaging*, *Physica Medica* **56** (Dec., 2018) 84.
- [19] V. Di Trapani, A. Bravin, F. Brun, D. Dreossi, R. Longo, A. Mittone et al., *Characterization of the acquisition modes implemented in Pixirad-1/Pixie-III X-ray Detector: Effects of charge sharing correction on spectral resolution and image quality*, *Nuclear Instruments and Methods in Physics Research Section A: Accelerators, Spectrometers, Detectors and Associated Equipment* **955** (Mar., 2020) 163220.
- [20] T. Schoonjans, A. Brunetti, B. Golosio, M. S. del Rio, V. A. Solé, C. Ferrero et al., *The xraylib library for X-ray–matter interactions. Recent developments*, *Spectrochimica Acta Part B: Atomic Spectroscopy* **66** (2011) 776–784.
- [21] H. Benaroya, S. M. Han and M. Nagurka, *Probability Models in Engineering and Science*. CRC Press, June, 2005.
- [22] G. Poludniowski, A. Omar, R. Bujila and P. Andreo, *Technical Note: SpekPy v2.0—a software toolkit for modeling x-ray tube spectra*, *Medical Physics* **48** (2021) 3630–3637.
- [23] R. Bujila, A. Omar and G. Poludniowski, *A validation of SpekPy: A software toolkit for modelling X-ray tube spectra*, *Physica Medica* **75** (July, 2020) 44–54.